THE JOURNAL OF PHYSICAL CHEMISTRY C

Article

pubs.acs.org/JPCC

First-Principles Investigation of NO_x and SO_x Adsorption on Anatase-Supported BaO and Pt Overlayers

Ruslan Hummatov,[†] Oğuz Gülseren,[‡] Emrah Ozensoy,[§] Daniele Toffoli,*[,∥] and Hande Üstünel*[,†]

[†]Department of Physics, Middle East Technical University, 06531 Ankara, Turkey
[‡]Department of Physics, Bilkent University, 06800 Bilkent, Ankara, Turkey
[§]Department of Chemistry, Bilkent University, 06800 Bilkent, Ankara, Turkey
[∥]Department of Chemistry, Middle East Technical University, 06531 Ankara, Turkey

S *Supporting Information*

ABSTRACT: We present a density functional theory investigation of the adsorption properties of NO and NO_2 as well as SO_2 and SO_3 on BaO and Pt overlayers on anatase $TiO_2(001)$ surface. Monolayers, bilayers, and trilayers of BaO grow without strain-induced large scale reconstructions. While the bilayer and trilayer preserve, to a large extent, the NO_2 adsorption characteristics of the clean BaO(100) surface, the effect of the support is evident in SO_2 and SO_3 adsorption energies, which are somewhat reduced with respect to the clean BaO(100) surface. When a Pt(100) layer is added on the TiO_2 surface, four stable adsorption geometries are identified in the case of NO while NO_2 is found to adsorb in only two configurations.

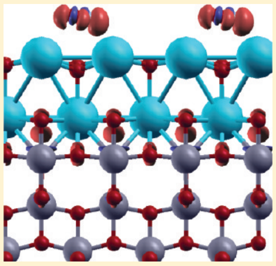

1. INTRODUCTION

While lean-burn diesel engines present a higher fuel efficiency, the traditional three-way catalytic converters, designed for stoichiometric fuel consumption, do not provide a sufficient elimination of pollutants such as NO_x (NO and NO_2) and hydrocarbons.[1] In 1994, Toyota designed a new heterogeneous catalyst that reduces the harmful NO and NO_2 gases to O_2, N_2 and hydrocarbons to CO_2 and water, before release into the atmosphere.[2] The NO_x *storage/reduction catalyst* (NSR) is a promising solution to the NO_x emission problem and has been the subject of a large amount of experimental[3−8] and theoretical[9−13] research aimed at its optimization. These efforts have been largely motivated by the restrictions and goals for NO_x emission put forward by various agencies around the world.[14]

The NO_x storage/reduction catalysts typically have three components. A precious metal, such as Pt, Rh, or Pd, catalyzes the oxidation reaction and converts most of the incoming NO into NO_2, which is more efficiently trapped in the storage component. The storage component is usually an alkaline earth metal oxide, such as BaO, which traps the NO_2 in the form of surface or bulk nitrates and nitrites. These two steps take place during a long *lean* period, followed by a brief, *fuel-rich* period, during which the stored nitrates are released and are converted into O_2 and N_2. This redox reaction is once again promoted by the precious metal. Upon release of the stored NO_x, the catalyst is regenerated and the cycle starts over. A third component, a second metal oxide, provides support to the entire system.

The most commonly preferred support material is γ-Al_2O_3 due to its open structure, thermal and mechanical integrity, as well as its favorable surface acidity.[15−17] Recently, however, new support materials have made their way into the literature either in their pure form or in mixture with other metal-oxides.[18,19] One such material is anatase TiO_2, having shown promising properties in several experimental studies,[20−22] most notably an improved sulfur tolerance with respect to γ-Al_2O_3 and the capability to control the BaO surface dispersion.[23] Sulfur deactivation occurs as a result of the high affinity of SO_2 and SO_3 species (SO_x), present in the exhaust products, for the storage material. SO_x poisons both the redox component and the support.[19,24] In particular, the formation of sulfates with the storage material inhibits the NO_x storage step, since the sulfates are more stable than nitrates.[20] In the present work, we investigate certain aspects of TiO_2 as a possible support material in the NO_x storage/reduction catalyst systems. To the authors' knowledge, this is the first theoretical study on this subject.

To assess the suitability of anatase as support material in NSR catalysts, it is important to characterize its interaction with the other components of the system. In the first part of this work, we investigate the interaction of the support material with the storage component. Due to the moderate lattice constant mismatch between the two materials, one, two, and three layers of BaO can grow on the surface without large distortions. We will therefore consider ordered layers of BaO(100) supported on the (001) surface of anatase TiO_2. We then investigate the interaction between TiO_2 and the redox component and how the support material influences the NO and NO_2 adsorption on the precious metal.

Received: September 12, 2011
Revised: February 9, 2012
Published: February 16, 2012

dx.doi.org/10.1021/jp208790a | *J. Phys. Chem. C* 2012, 116, 6191−6199

2. METHOD AND COMPUTATIONAL DETAILS

The calculations presented in this work were performed using plane-wave pseudopotential density functional theory[25,26] with the gradient-corrected approximation (GGA). The Perdew−Becke−Ernzerhof[27] exchange-correlation functional as implemented in Quantum-Espresso[28] was used in all calculations. The open-source program XCrysDen[29] was used for visualization and to produce the figures. During the BFGS geometry optimizations, a force threshold per atom of 0.025 eV/Å was used. The use of ultrasoft pseudopotentials[30] to model the interaction between atomic nuclei and electrons allows an affordable kinetic energy cutoff of 40 Ryd and a density cutoff of 400 Ryd.

Anatase has a tetragonal cell with 4 TiO_2 units in the unit cell. A variable-cell relaxation is performed with a 10 × 10 × 5 Monkhorst−Pack[31] *k*-point mesh. Calculated cell parameters (a = 3.786 Å, c = 9.619 Å) are in good agreement with experimental values (3.782 Å, 9.502 Å[32]) and previous theoretical (3.786 Å, 9.737 Å[33,34]) calculations.

Clean anatase (001) surfaces are modeled by periodically repeated slabs with atomic positions that are obtained from the bulk. A suitable number of layers are fixed from the bottom to mimic bulk behavior, resulting in an asymmetric slab. Surface energies are then calculated as detailed in ref 35. As a check, we calculated the surface energy of a six-layer slab with all layers free and obtained a value of 0.89 J/m^2, in excellent agreement with Lazzeri et al.[33,34] A convergence study revealed that a good compromise between accuracy and computational cost is obtained by using a four-layer slab with the bottom two layers fixed, yielding a surface energy of 0.89 J/m^2. In order to minimize interactions between periodic images, the calculations are performed with a vacuum of approximately 12−13 Å between slabs. The absence of dipole interaction between slabs is checked by using larger values for the vacuum.

All clean surfaces are studied in a 1 × 1 surface slab geometry with a *k*-point mesh of 6 × 6 × 1. All molecular adsorption energies are studied in a $\sqrt{2} \times \sqrt{2}$ supercell with a 3 × 3 × 1 mesh. To study the effect of coverage on adsorption energies, NO_x and SO_x adsorption has been studied for both the $\sqrt{2} \times \sqrt{2}$ and 2 × 2 supercells on bare BaO(100) (see Figure 1).

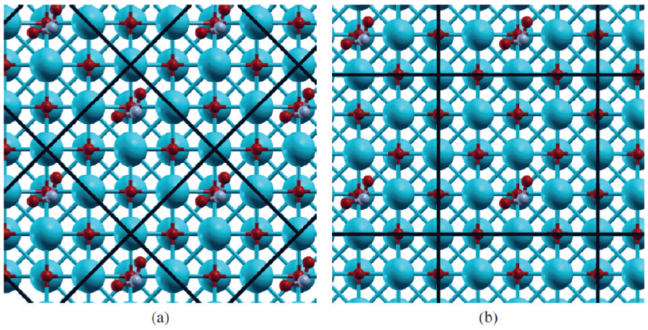

Figure 1. Flat NO_2 adsorption configuration on bare BaO(100), (a) in a $\sqrt{2} \times \sqrt{2}$ unit cell ($^1/_4$ coverage) and (b) in a 2 × 2 unit cell ($^1/_8$ coverage).

Marzari−Vanderbilt[36] smearing has been used, where applicable, with a width of 0.01 and 0.02 Ryd. Spin polarization was employed as needed.

The calculated lattice parameter of BaO (5.582 Å) agrees well with the experimental value of 5.523 Å[37] and theoretical estimate of 5.608 Å reported by Schneider.[38] A similar convergence test as was conducted for the TiO_2(001) surface reveals that a five-layer slab with the two bottom layers fixed is a suitable model for the BaO(100) surface. The calculated surface energy of 0.31 J/m^2 for this model is in good agreement with previously reported theoretical values (0.35[38] J/m^2 and 0.4[39] J/m^2). In general, the presence of unsaturated bonds is the main reason of surface reactivity. During geometric optimization surface oxygens move inward causing a mild surface reconstruction referred to as "rumpling". Computed rumpling and relaxation of this surface are in good agreement with reported values.[39,40]

Finally, distances and angles associated with the molecules considered for adsorption, namely NO, NO_2, SO_2, and SO_3, were calculated in a large cubic supercell. For NO, the calculated bond length is 1.167 Å. Both NO_2 and SO_2 have a bent structure; the bond lengths are 1.212 and 1.459 Å while the angles are 133.9° and 119.3°, respectively. SO_3 has a trigonal planar structure with an S−O bond length of 1.448 Å. All of the calculated values compare favorably with previous theoretical and experimental gas phase results.[38]

The binding energy of the adsorbed species is calculated using the formula

$$E_b = E_{tot}^{surf+ad} - E_{tot}^{surf} - E_{tot}^{ad} \tag{1}$$

where $E_{tot}^{surf+ad}$ is the total energy of the full system (surface + adsorbate), E_{tot}^{surf} is the energy of the bare surface, and E_{tot}^{ad} is the energy of the gas phase molecules. According to this definition, the binding energies of stable adsorbates are negative; however, as a matter of convenience we only report their magnitudes. Thus, the higher the binding energy quoted the more strongly bound the species is to a surface.

Adhesion energies of BaO overlayers on TiO_2(001) have been calculated using the formula

$$E_{adh} = E_{tot}^{TiO_2+BaO} - E_{tot}^{TiO_2} - E_{tot}^{BaO} \tag{2}$$

where $E_{tot}^{TiO_2+BaO}$ is the total energy of the BaO overlayer on the TiO_2(001) slab, $E_{tot}^{TiO_2}$ is the total energy of the pristine TiO_2(001) slab, and E_{tot}^{BaO} is the total energy of the isolated overlayers calculated at their optimum lattice constant. Thus, the adhesion energies reported in Table 1 include the readjustment of the overlayers to the lattice constant of TiO_2.

Table 1. Lattice Constants, Percent Mismatches of the Isolated Monolayer, Bilayer, and Trilayer, and Their Adhesion Energies to the TiO_2(001) Surface[a]

	monolayer I	monolayer II	bilayer	trilayer
lattice constant (Å)	5.29	5.29	5.44	5.45
percent mismatch (%)	4.48	4.48	1.63	1.33
adhesion energies (J/m^2)	0.41	1.78	1.23	1.52

[a] Lattice constants are in Å and adhesion energies are in J/m^2.

3. RESULTS AND DISCUSSION

3.1. BaO Overlayers on TiO_2(001) Surface.

When the theoretical values for the lattice constants of BaO and anatase TiO_2 are taken into account, BaO(100) and TiO_2(001) surfaces display a lattice mismatch of approximately 4% when held at a relative angle of 45°. This moderate lattice mismatch suggests that growth of a few ordered layers of BaO(100) on TiO_2(001) is possible. In order to verify this expectation, we placed a single

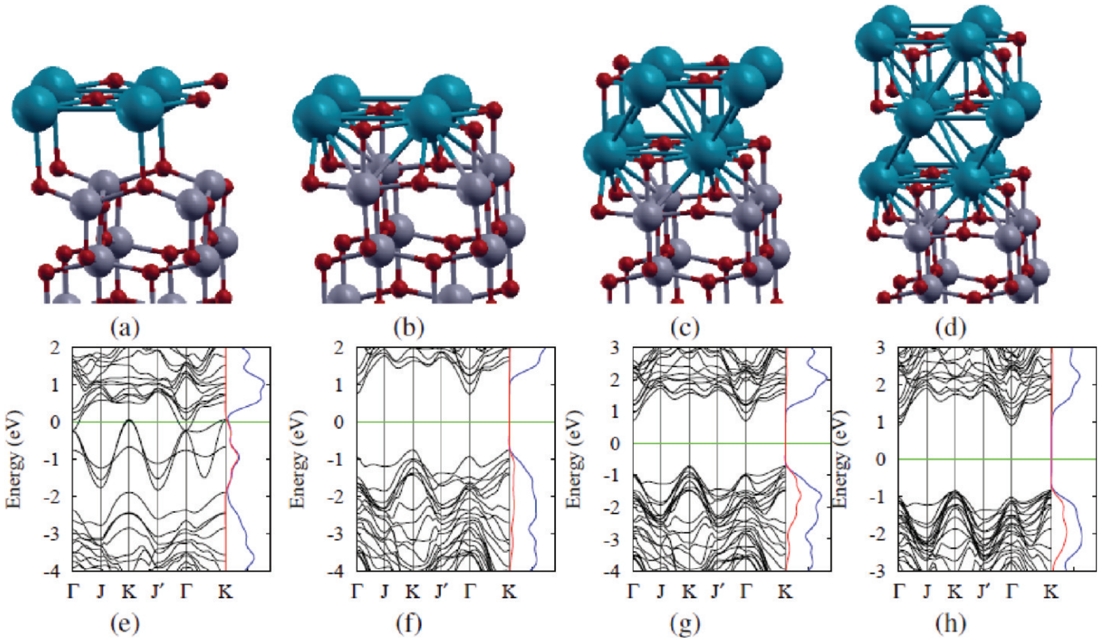

Figure 2. (a) Type I and (b) type II monolayers, (c) BaO bilayer and (d) trilayer. (e−h) For each system, the band structure and the PDOS analysis are reported below the corresponding figures. The blue curve in the PDOS plots is the total density of states of the whole system, and the red curve is the PDOS of the layer alone. Ba atoms are shown in blue, O in red, and Ti in gray.

monolayer of BaO(100) on the relaxed $TiO_2(001)$ surface, decreasing the BaO lattice constant appropriately to match that of the underlying surface. Subsequent geometric optimizations starting from several initial separations between the monolayer and the surface yield two final configurations, referred to as type I monolayer and type II monolayer in the following and depicted in Figure 2a,b. The type I monolayer is loosely bound to the anatase surface with a distance of 2.82 Å. An analysis of the band structure and partial density of states (PDOS), reported in Figure 2e, reveals that the BaO states are localized in the band gap with little or no perturbation to the band structure of the pristine $TiO_2(001)$ surface. This result is expected due to the weak binding of the monolayer to the surface as suggested by its large separation.

The second configuration, shown in Figure 2b, presents a second possibility where the monolayer is located only 2.03 Å above the surface. The band structure and the accompanying PDOS analysis presented in Figure 2f display, as a result of the strong interaction in this case, the complete assimilation of the BaO states into the valence and conduction bands of TiO_2. Thus, the combined structure remains a semiconductor. The well-known *rumpling* of the BaO(100) surface[39] takes place on a much smaller scale for the monolayers. While the difference between the vertical heights of anions and cations is found to be 0.12 Å for the clean BaO(100) surface, this difference is reduced to 0.02 and 0.06 Å for type I and type II monolayers, respectively. The surface energy difference between the two types of monolayers is 1.33 J/m^2 with type II being more stable. For reference, the surface energies of the (111) and (100) surfaces of Si are 1.14[41] and 2.13[42] J/m^2.

At this point it is instructive to explore the transition from overlayer behavior to bulk behavior as a function of number of layers. As a first step, we place a second layer on both the type I and type II monolayers. Geometric optimization of the bilayer grown on type I BaO monolayer results in the detachment of the bilayer from the surface, causing the structure to break down. This is expected due to the stronger BaO interlayer interaction as compared to the considerably weaker attraction between the surface and the first BaO layer. On the other hand, the growth of a second layer on the type II monolayer is achieved as displayed in Figure 2c,g along with the band structure and PDOS analyses. The shortest distance between the two BaO layers is calculated to be 2.90 Å. This value is comparable to the interlayer separation of 2.79 Å in bulk BaO. The shortest distance between the bottom layer and the surface is 2.08 Å, and this distance is almost unchanged in the transition from the type II monolayer to the bilayer. As revealed by the band structure analysis, all the BaO contribution remains localized inside the valence band of TiO_2. This aspect of the bilayer is reminiscent of the type II monolayer.

Finally, a third layer is added on top of the bilayer. The optimized geometry and band structure analysis are reported in Figure 2d,h. In spite of the expectation of convergence toward bulk behavior, the three overlayers form a staggered pattern of large and small interlayer distances. The shortest distances between consecutive layers are, starting from the bottom, 2.05, 3.02, and 2.63 Å, respectively. This alternating behavior can be understood once again in terms of competing BaO interlayer interaction and the strong BaO−surface interaction. The electronic structure is still similar to the type II monolayer, with the BaO states incorporated into those of TiO_2 as apparent from Figure 2h.

The adhesion energies of the BaO overlayers on TiO_2 are reported in Table 1, along with the optimized lattice constants of the isolated overlayers and their percent mismatch with respect to the TiO_2 (001) surface. Type I monolayer could be of particular importance as it corresponds to a BaO layer that is relatively weakly bound to the underlying TiO_2 substrate. It is experimentally well-established that BaO overlayers on metal oxide substrates can readily experience morphological changes and surface reconstructions depending on BaO coverage, temperature, or the presence of adsorbates such as NO_2 or H_2O.[17,43] As a result, BaO mono/multilayers can reversibly wet (disperse) or dewet (sinter) the metal oxide support at different conditions. Along these lines, type I monolayer is a relevant model for the initial stages of BaO sintering on a metal oxide support.

For all overlayers, with the exception of monolayer I, the adhesion energies are quite large, as a result of a strong interaction with the TiO_2 substrate. This observation points toward the thermodynamic stability of the supported overlayers. As defined in eq 2, these adhesion energies include the readjustment of the overlayers to the lattice constant of the TiO_2 support. In going from the bilayer to the trilayer, the adhesion energy is seen to increase in line with the smaller lattice mismatch. These observations support recent experimental studies on $BaO/TiO_2/Pt(111)$ planar model catalysts[44] where it was shown via X-ray photoelectron spectroscopy (XPS) that there exists a strong interaction between the top BaO_x overlayer and the underlying TiO_2 substrate. Such a strong $BaO-TiO_2$ interaction is also in agreement with former reports on high surface area $BaO/TiO_2/Al_2O_3$ ternary mixed oxide systems which reveal a preferential and strong binding of BaO sites on TiO_2 domains.[23]

3.2. NO_x and SO_x Adsorption Characteristics on BaO Overlayers. Any candidate system for sulfur poisoning reduction is expected to satisfy two conditions: while decreasing the adsorption energies of SO_x species on the most populated adsorption sites, the new material should not cause a deterioration of the NO_2 adsorption energies for the same sites. To explore this, we study the high-stability NO_2, SO_2, and SO_3 binding sites previously identified by Schneider[38] on the bare BaO(100) surface. The optimized geometries of the adsorbates on the various BaO overlayers described above are displayed in Figures 3 and 4. The three configurations identified for NO_2 adsorption reduce to a single geometry for the SO_2 molecule after optimization. For all adsorbates and adsorption geometries, selected geometrical parameters are included in the Supporting Information.

SO_2 and SO_3 behave as Lewis acids (i.e., electron density acceptors) and bind preferentially to the surface oxygen sites to form sulfites and sulfates, respectively. NO_2, on the other hand, is amphiphilic and can bind to the surfaces in three different modes: acid-like N-down, base-like with the oxygens bridging two metal sites, and flat. The adsorption energies of NO_2 on BaO(100) surface compare well with previous theoretical results.[38,39,45]

The effect of coverage on the computed adsorption energies has been investigated for NO_x and SO_x adsorption on bare BaO (100) surface. Adsorption energies for two coverages, $\theta = {}^1/_4$ and $\theta = {}^1/_8$, corresponding to $\sqrt{2} \times \sqrt{2}$ and 2×2 supercells (see Figure 1) are reported in Table 2. While the adsorption energies of NO_2 are not appreciably affected, SO_2 and SO_3 binding energies decrease by about 0.3 eV with increasing coverage. In the following discussion on BaO overlayers, NO_2 and SO_x adsorption energies correspond to $\theta = {}^1/_4$.

For both NO_2 and SO_x, our adsorption geometries compare very well with the work of Schneider.[38] This applies to both the bare BaO(100) surface and the supported overlayers. The binding energies on the overlayers are reported in Table 3 and compared with the binding energies of the corresponding geometries on the bare BaO(100) surface.

The adsorption energy for the N-down configuration of NO_2 (first column of Figure 3, see also Table 3) is strongly dependent on the type of overlayer, the largest being for the type I monolayer. The adsorption energy of this configuration for the other overlayers is sizably smaller. The flat and bridge geometries have similar adsorption energies on the bare BaO(100) surface and type II monolayer while the flat configuration is more strongly adsorbed on the type I

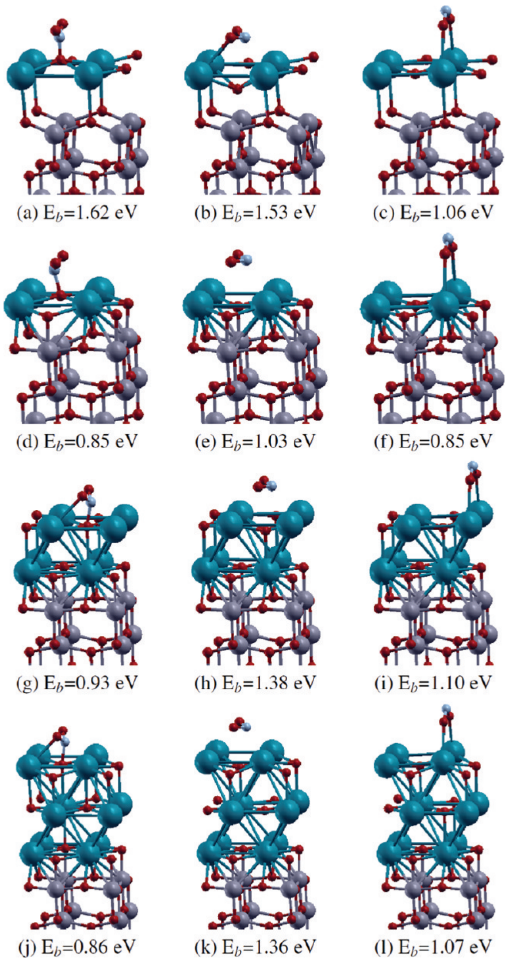
(a) E_b=1.62 eV (b) E_b=1.53 eV (c) E_b=1.06 eV
(d) E_b=0.85 eV (e) E_b=1.03 eV (f) E_b=0.85 eV
(g) E_b=0.93 eV (h) E_b=1.38 eV (i) E_b=1.10 eV
(j) E_b=0.86 eV (k) E_b=1.36 eV (l) E_b=1.07 eV

Figure 3. Three NO_2 adsorption configurations (a–c) on BaO monolayer type I, (d–f) on BaO monolayer type II, (g–i) on bilayer BaO, and (j–l) on trilayer BaO. Ba atoms are shown in blue, O in red, N in light blue, and Ti in gray.

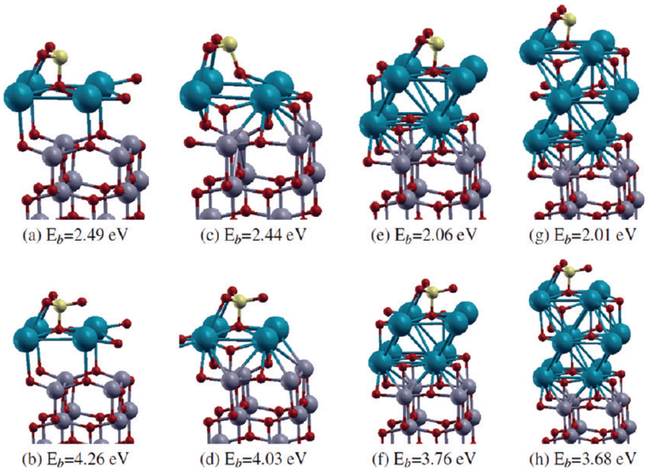
(a) E_b=2.49 eV (c) E_b=2.44 eV (e) E_b=2.06 eV (g) E_b=2.01 eV
(b) E_b=4.26 eV (d) E_b=4.03 eV (f) E_b=3.76 eV (h) E_b=3.68 eV

Figure 4. SO_2 and SO_3 adsorption geometries (a, b) on BaO monolayer type I, (c, d) on BaO monolayer type II, (e, f) on bilayer BaO, and (g, h) on trilayer BaO. Ba atoms are shown in blue, O in red, S in yellow, and Ti in gray.

Table 2. Adsorption Energies of NO_2, SO_2, and SO_3 on Bare BaO(100) Surface in $\sqrt{2} \times \sqrt{2}$ and 2 × 2 Supercells, Corresponding to Coverages of $\theta = {}^{1}/_{4}$ and $\theta = {}^{1}/_{8}$, Respectively[a]

adsorption geometry	$\theta = {}^{1}/_{4}$	$\theta = {}^{1}/_{8}$
NO_2 N-down	1.19	1.11
NO_2 flat	1.09	1.08
NO_2 bridge	0.97	1.01
SO_2	2.34	2.66
SO_3	4.05	4.37

[a] All binding energies are in eV.

Table 3. Adsorption Energies of NO_2, SO_2, and SO_3 on Bare BaO(100) Surface, BaO Monolayer Type I and Type II, Bilayer BaO, and Trilayer BaO[a]

adsorption geometry	BaO(100)	type I ML	type II ML	bilayer	trilayer	isolated bilayer
NO_2 N-down	1.19	1.62	0.85	0.93	0.86	1.03
NO_2 flat	1.09	1.53	1.03	1.38	1.36	1.30
NO_2 bridge	0.97	1.06	0.85	1.10	1.07	1.14
SO_2	2.34	2.49	2.44	2.06	2.01	2.29
SO_3	4.05	4.26	4.03	3.76	3.68	3.98

[a] Binding energies for an isolated BaO bilayer are also presented for comparison. All binding energies are in eV.

monolayer, bilayer, and trilayer. Overall, for the acidic adsorbates SO_2 and SO_3, the adsorption energies are significantly larger than those of NO_2. However, a clear trend of decreasing adsorption energies is observed with increasing BaO thickness of the overlayers.

The first column of Figure 3 shows the N-down binding configuration of the NO_2 molecule on the overlayers discussed above. In all instances, a Bader charge analysis reveals a partial positive charge localization on the surface oxygen directly below the N atom of the molecule. The adsorption geometry of NO_2 on the type I monolayer is markedly different from the other cases (Figure 3a). The O_{surf}–NO_2 fragment is planar with an N–O_{surf} distance of 1.34 Å and an N–O distance of 1.25 Å. The O–N–O_{surf} and the O–N–O angles are 117.3° and 125.4°, respectively. This geometry suggests the formation of a nitrate. The binding energy of 1.62 eV is close to the value calculated previously for the isolated BaO monolayer (1.53 eV).[46] In all other BaO overlayers, the molecule acquires about 0.8 |e| of charge upon adsorption. The geometry of the NO_2 fragment which deviates considerably from the gas phase geometry of the nitrite anion signals the formation of a NO_3^{2-} species as is also evident from an inspection of the spin density. The binding energy of the NO_2 in the N-down configuration is similar in the type II monolayer, bilayer, and trilayer.

The flat adsorption geometry, seen in Figure 3b,e,h,k, is sometimes referred to as "ionic" since the interaction with the alkaline earth oxide is nondirectional and is mainly electrostatic in nature.[38] The geometry of the adsorbate is close to that of a gas-phase nitrite anion, while a Bader charge analysis reveals that, upon adsorption, an electronic hole is delocalized over the oxide anions. The pure electrostatic nature of the bond between the adsorbates and the surface is clearly apparent from the density difference plot displayed in Figure 5. An interpretation of the observed trend in adsorption energy can be obtained from geometric considerations. In each of the four BaO overlayers, the molecule rests with its two oxygens directly above a surface oxygen. In the type I monolayer, the surface oxygen moves downward, thus decreasing the electronic repulsion which results in a higher binding energy. In the type II monolayer and to a certain extent in the bilayer case, the surface oxygen has relatively limited freedom due to the reduced distance between the two topmost layers. The repulsion between the molecular and surface oxygens then drives the molecule away from the surface. In the bridge configuration, displayed in Figure 3c,f,i,l, the NO_2 molecule interacts with the surfaces through its two oxygens. The binding energies in this case are rather insensitive to the particular overlayer. Similarly to the flat adsorption geometry, the adsorbate can be regarded as a nitrite, and with a similar delocalization of a positive partial charge on the surface.

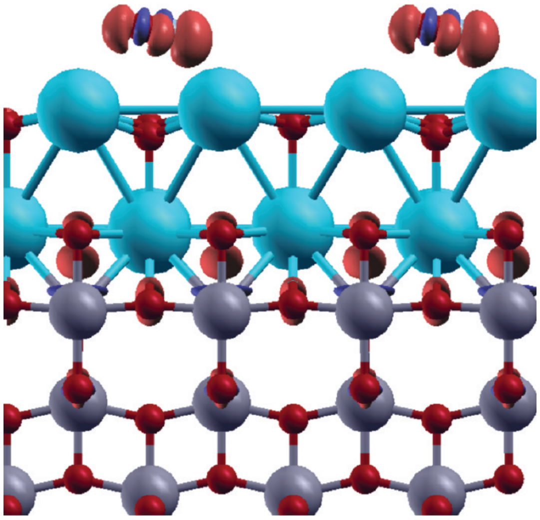

Figure 5. Charge density difference contour obtained by taking the difference of the electron density of NO_2 adsorbed on the supported bilayer in the flat configuration and those of the isolated components, namely NO_2, the bilayer, and the TiO_2 slab. Electron-deficient regions are blue while those with an excess of electronic density are red.

It is worth noting that the improved NO_2 adsorption properties of the type I monolayer in comparison to the bare BaO surface is at least in part due to the electronic properties of the isolated BaO monolayer.[46] In all the supported overlayers, the *flat* and *bridge* configurations retain their geometry while displaying an increase in the binding energies of about 0.35 and 0.25 eV, respectively, in going from the type II monolayer to the supported bilayer. This increase is most likely due to the increased separation between the top and bottom BaO layers, which partially brings back the local environment observed in the type I monolayer.

The binding energies of SO_2 and SO_3 on the bare BaO(100) surface and various BaO overlayers display an interesting trend. In going from the bare BaO(100) surface to the bilayer, there is a substantial decrease of 0.3 eV in binding energies for both adsorbed species. No significant variation is observed in going from the bilayer to the trilayer. On the other hand, the adsorption energies on both type I and type II monolayers are generally higher than those on BaO(100) and the supported bilayer. An insight into the role played by the anatase support is provided by comparing the adsorption energies on the supported bilayer and an isolated bilayer reported in Table 3. Since the adsorption energies on the isolated bilayer are similar to those on bare BaO(100), we conclude that the role of the support is to destabilize to a certain extent the sulfur species. In order to characterize the importance of lattice strain, the SO_2 binding energy on the clean BaO(100) surface in a 2 × 2 supercell was recalculated fixing the lattice constant to the smaller value used in the overlayer calculations (5.358 Å) and was found to decrease by only 0.12 eV. The lattice strain therefore accounts for part of the reduced stability of the sulfur species on the supported overlayers. A partial density of states (PDOS) and charge density difference analysis has been carried out in order to characterize the electronic reason that would account for the destabilizating role of the TiO_2 support on the SO_2 and SO_3 bonding. The results of this analysis, included in the Supporting Information, reveal no change in the nature of the adsorbate/surface bonding in going from the bare BaO(100) surface to the supported BaO overlayers. The reduction of the binding energy of SO_x species on the supported bilayer and trilayer beyond the effect of lattice strain must therefore be attributed to differences in structural properties. For SO_2, the average distance between the O_{surf} directly bonded to S and the nearest surface Ba atoms increases from 2.78 to 2.92 Å in going from the supported bilayer to the bare BaO(100) surface, resulting in diminished SO_2 binding on the supported bilayer with respect to bare BaO(100). A similar near-detachment of the surface O is observed also for SO_3 in line with the reduction observed in the binding energy.

Several conclusions can be drawn from this study. Of the two monolayers, only the type I is a promising candidate for a storage component with strengthened adsorption of NO_2 species although it is not appreciably more resilient toward SO_x adsorption. On the other hand, the bilayer and trilayer show a favorable reduction of affinity for SO_2 and SO_3 adsorption while improving, to a certain extent, the NO_2 adsorption energies of the bare BaO(100) surface. These results are also in good agreement with recent experimental studies on NO_x[23] and SO_x[47] adsorption on $BaO/TiO_2/Al_2O_3$ ternary oxide systems indicating the presence of strong NO_x binding sites which can also be thermally regenerated much more efficiently after sulfur poisoning than the conventional BaO/Al_2O_3 system which does not contain a TiO_2 promoter. In these experimental studies, it was reported that the total SO_x uptake of the $BaO/TiO_2/Al_2O_3$ system at room temperature was much higher than the Ti-free BaO/Al_2O_3 binary mixed oxide system. On the other hand, at elevated temperatures SO_x desorption and release from the $BaO/TiO_2/Al_2O_3$ system was much more facile than that of BaO/Al_2O_3. In other words, in spite of the significantly larger SO_x storage on the $BaO/TiO_2/Al_2O_3$ system, this surface could be effectively regenerated via thermal SO_x desorption while BaO/Al_2O_3 system storing a lesser extent of SO_x is poisoned in an almost completely irreversible fashion. In the light of the DFT results presented above, it can be argued that, during the low-temperature SO_x adsorption on $BaO/TiO_2/Al_2O_3$ surface, SO_x adsorption preferentially occurs on type II monolayer-like 2-D BaO islands (Figure 2b). Due to the stronger SO_x binding on these sites (Table 3), SO_x storage is enhanced. During thermal regeneration at elevated temperatures (e.g., 950 K), BaO domains on the $BaO/TiO_2/Al_2O_3$ surface sinter forming larger 3-D clusters such as the bilayer and trilayer structures given in Figure 2c,d, respectively. Since the stability of SO_x species on the bilayer and trilayer structures are reduced with respect to the type II monolayer (Table 3), SO_x desorption can occur enabling efficient desulfurization of the $BaO/TiO_2/Al_2O_3$ surface.

3.3. Pt Monolayer on TiO_2.

In order to further explore the characteristics of $TiO_2(001)$ as a support material, we investigate its interaction with Pt, the most commonly used noble metal in NSR catalysts (Figure 6). As in the case of BaO, Pt may be adsorbed on the surface in the form of single atomic species, clusters, and extended geometries. The lattice constant of bulk Pt was calculated to be 4.00 Å in excellent agreement with Getman and Schneider.[48] The lattice mismatch between anatase and Pt is about 5% for the same 45°-rotated structure of the (100) surface which lends itself easily to monolayer growth. The Pt monolayer is initially prepared as a simple flat layer on TiO_2, with the Pt atoms on top of the oxygen atoms. During geometric optimization, the monolayer undergoes a sizable reconstruction. The deformation is a combination of a rumpling and a sliding of the top layer with respect to the surface so that the Pt atoms are no longer on top of the surface atoms. Due to rumpling, alternating Pt atoms have an average distance of 2.22 and 2.75 Å from the anatase surface. This reconstruction was found to be independent of the initial configuration of the Pt overlayer.

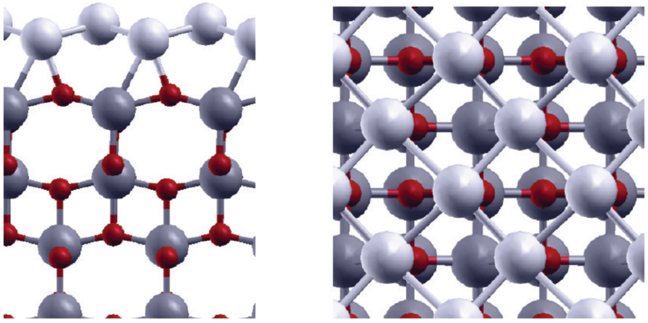

Figure 6. (Left) Side view and (right) top view of the Pt overlayer on anatase $TiO_2(001)$. O atoms are shown in red, Ti in gray, and Pt in white.

Since Pt catalyzes the oxidation of NO to NO_2, which precedes the storage, an important initial step is to understand the adsorption geometries of NO and NO_2 molecules on the Pt monolayer. Previous studies on pure precious metal surfaces have identified the NO adsorption geometry as perpendicular to the surface with the N atom pointing down.[48−50] In the case of the monolayer at hand, more adsorption configurations are possible due to the richer topology of the surface. We explore several different initial configurations, among which are atop and hcp geometries. The optimized geometries do not retain the simple linear alignment of the NO molecule as seen in Figure 7. The adsorption of the NO species induce a further, rather large surface reconstruction that disturbs the puckering order causing the Pt atoms to be organized into semiregular clusters. Of the four optimized adsorption geometries, two have correspondence to NO adsorption on clean Pt(111) surface as reported by Getman and Schneider.[48] The least stable configuration corresponds to an O-down bent atop geometry with a binding energy of 1.44 eV (Figure 7a) and with a negligible charge transfer between the surface and the molecule. This configuration has not been previously observed on pristine Pt(111) surface. A much larger adsorption energy (2.62 eV) is observed for the N-down bent atop geometry (Figure 7b), which is essentially the same configuration as identified by Getman and Schneider,[48] and it is characterized by a charge transfer of 0.12 |e| from the surface to the molecule. We also

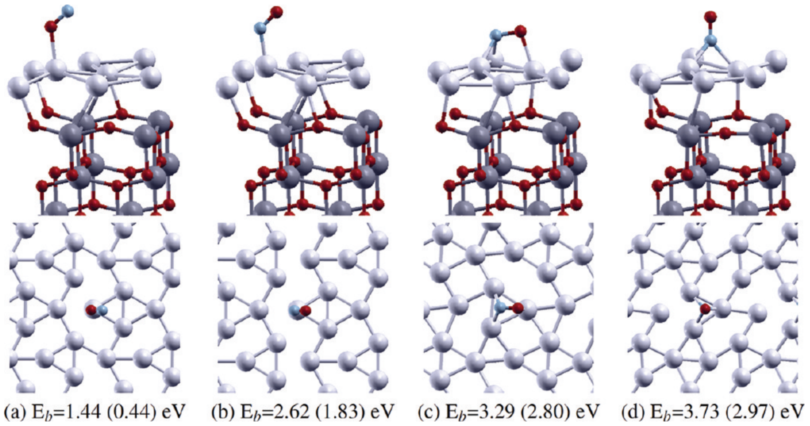

Figure 7. Relaxed NO configurations on the Pt overlayer (side view on the top panel and top view on the bottom panel): (a) O down, (b) N down, (c) bridge, and (d) N-down hollow site. Only the Pt layer is shown in the bottom panel. The binding energies recalculated by replacing the third term in eq 1 with the scf (single-point) energy of the reconstructed slab are reported in parentheses. O atoms are shown in red, Ti in gray, N in light blue, and Pt in white.

note that the distribution of charge between N and O somewhat differs from the gas phase distribution. Another stable adsorption geometry corresponds to an NO fragment almost parallel to the surface with the N atom bridging two Pt atoms (Figure 7c). Similarly to the O-down configuration, this geometry has also not been observed on the Pt(111) surface although it has a rather large binding energy of 3.29 eV on the Pt monolayer. Bader charge analysis reveals a charge transfer of 0.51 |e| from the surface to the molecule for this configuration. In the most stable adsorption geometry NO binds vertically on a hollow site as seen in Figure 7d. The binding energy for this configuration was previously reported to range between 1.44 and 2.02 eV[9,49,50] on the metallic Pt(111) surface. Our own calculations for the same configuration in a 3 × 3 five-layer Pt(111) surface give a binding energy of 1.96 eV, consistent with this range. The computed binding energy of 3.73 eV is much higher than the binding energy computed on pristine Pt(111) surface. However, the computed N−O distance of 1.203 Å compares reasonably well with the N−O distance in the hcp- and fcc-bound configurations reported in ref 48. The elongation of the N−O bond during adsorption is computed to be around 0.04 Å in excellent agreement with Getman and Schneider.[48] A Bader charge analysis predicts a charge transfer of 0.41 |e| from the surface to the adsorbate.

During the addition of NO, the monolayer is seen to undergo large scale reconstructions, which contribute to the binding energies calculated using eq 1. In order to separate this effect from the actual NO adsorption, the binding energies have been recalculated replacing the third term in eq 1 with the single-point self-consistent field energy of the reconstructed slab (obtained by removing the NO molecule from the fully relaxed system in each case). These values are included in paranthesis in Figure 7. This correction, although sizable, does not alter the relative stabilities of the adsorbed geometries.

NO_2 adsorption on the Pt monolayer occurs in a limited number of configurations, in comparison to the NO adsorption. All of the initial NO_2 configurations relax to one of the two optimized geometries depicted in Figure 8. The binding energy of the O-down bridge configuration is 4.07 eV (Figure 8a). Both N−O bonds have a length of 1.27 Å while the O−N−O angle is 121.6° and consistent with the gas phase geometry of a nitrite. A Bader charge analysis reveals accordingly a substantial charge transfer (0.5 |e|) from the surface to the adsorbate. The adsorption energy of the N−O bridge configuration, the so-called μ-N,O-nitrito, is 3.21 eV (Figure 8b). Upon adsorption, the N−O bond that lies parallel to the surface is lengthened by 0.11 Å while the free N−O bond length remains unchanged. The O−N−O angle decreases by about 15°, in perfect agreement with Getman and Schneider.[48] This last configuration may be located in several different points on the surface, and the energy differences are within about 0.25 eV of each other depending on the location. The binding energies corrected for the large reconstruction upon adsorption are once again given in paranthesis in Figure 8. The N-down nitro configuration identified by Getman and Schneider[48] is not a stable configuration and relaxes to μ-N,O-nitrito after geometry optimization. It is also worth noting that μ-N,O-nitrito is not the most stable adsorption configuration at variance with the case of pristine Pt(111) surface.[48] The relative stabilities of the different configurations on pristine Pt(111) surface are known to be sensitive to surface coverage,[48] which could also affect the predictions of this work.

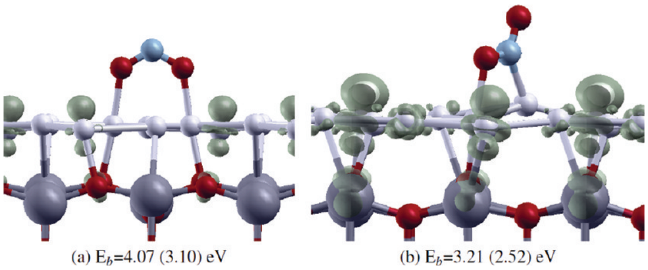

Figure 8. (a) O,O′-nitrito and (b) μ-N,O-nitrito configurations on Pt monolayer. The spin density is also plotted. The binding energies recalculated by replacing the third term in eq 1 with the scf (single-point) energy of the reconstructed slab are reported in parentheses. O atoms are shown in red, Ti in gray, N in light blue, and Pt in white.

4. CONCLUSIONS

Due to its sulfur-resilient properties, TiO_2 has found place in NSR catalysts along with more traditional support materials. In spite of the recent upsurge of experimental activity involving TiO_2, an atomistic interpretation of its interaction with the other components of the catalyst is still missing. We present a density functional theory investigation of the adsorption properties of NO and NO_2 on BaO and Pt overlayers on anatase $TiO_2(001)$ surface.

The small lattice mismatch between the (001) surface of anatase TiO_2 and the (100) surface of BaO allows monolayers, bilayers, and trilayers to grow without strain-induced large scale reconstructions. Two different types of monolayers were identified. The type I monolayer is weakly bound to the underlying surface with a large separation while the type II monolayer is bound more strongly. The bilayer and trilayer could only be stabilized over the type II monolayer. Type I monolayer displays a large affinity toward NO_2 due to its resemblance to an isolated BaO monolayer. Type II monolayer as well as the bilayer and trilayer preserve, to a large extent, the NO_2 adsorption characteristics of the clean BaO(100) surface. The effect of the support is more evident in SO_2 and SO_3 adsorption characteristics. The binding energies of these species on the bilayer and trilayer are somewhat reduced with respect to the clean BaO(100) surface.

When a Pt(100) layer is added on the TiO_2 surface, we observe large scale reconstructions, possibly due to the slightly larger lattice strain. For both NO and NO_2, the adsorption characteristics differ from those on a pristine Pt(111) surface. In addition to the two previously identified adsorption geometries on Pt(111), two other stable adsorption geometries are identified in the case of NO while NO_2 is found to adsorb in only two configurations. We note that the μ-N,O-nitrito is no longer the most stable configuration.

Several extensions of this study are possible. The computed NO and NO_2 adsorption energies and geometries will be used for a detailed investigation of the reaction mechanism of the NO oxidation step on TiO_2-supported Pt monolayers. Furthermore, while this study is focused on overlayers corresponding to large BaO and Pt loading percentages, future work will explore the stability of BaO and Pt clusters on various surfaces of TiO_2 and their affinity to NO_x and SO_x.

■ ASSOCIATED CONTENT

Supporting Information

Adsorption geometries for all adsorbates, Bader charge analysis, charge density difference, and partial density of states for SO_2 adsorption. This information is available free of charge via the Internet at http://pubs.acs.org.

■ AUTHOR INFORMATION

Corresponding Author

*E-mail: dtoffoli@metu.edu.tr (D.T.); ustunel@metu.edu.tr (H.U.).

Notes

The authors declare no competing financial interest.

■ ACKNOWLEDGMENTS

This work is financially supported by TÜBITAK, Scientific and Technological Research Council of Turkey (Grant 108T706). The computational resources were provided by ULAKBIM-GRID and UYBHM, National Center for High Performance Computing, located at Istanbul Technical University (Grant 10922010). E.O. acknowledges the Scientific and Technical Research Council of Turkey (TUBITAK) (Project 107Y115) and Turkish Academy of Sciences (TUBA) (Outstanding Young Investigator Grant) for financial support.

■ REFERENCES

(1) Matsumoto, S.; Takeuchi, M. *Top. Catal.* **2004**, *28*, 151.

(2) Matsumoto, S.; Yokota, K.; Doi, H.; Kimura, M.; Sekizawa, K.; Kasahara, S. *Catal. Today* **1994**, *22*, 127–146.

(3) Kwak, J.; Kim, D.; Szailer, T.; Peden, C.; Szanyi, J. *Catal. Lett.* **2006**, *111*, 119–126.

(4) Su, Y.; Kabin, K. S.; Harold, M. P.; Amiridis, M. D. *Appl. Catal., B* **2007**, *71*, 207.

(5) Piacentini, M.; Maciejewski, M.; Baiker, A. *Appl. Catal., B* **2007**, *72*, 105–117.

(6) Kim, J.-G.; Lee, H.-M.; Lee, M.-J.; Lee, J.-H.; Kim, J.-G.; Jeon, J.-Y.; Jeong, S.-K.; Yoo, S.-J.; Kim, S.-S. *J. Ind. Eng. Chem.* **2008**, *14*, 841–846.

(7) Sakamoto, Y.; Matsunaga, S.; Okumura, K.; Kayama, T.; Yamazaki, K.; Takahashi, N.; Tanaka, T.; Kizaki, Y.; Motohiro, T.; Shinjoh, H. *Chem. Eng. Sci.* **2008**, *63*, 5028–5034.

(8) Kim, D. H.; Chin, Y.-H.; Muntean, G. G.; Yezeretz, A.; Currier, N. W.; Epling, W. S.; Chen, H.-Y.; Hess, H.; Peden, C. H. F. *Ind. Eng. Chem. Res.* **2006**, *45*, 8815–8821.

(9) Jelic, J.; Meyer, R. J. *Catal. Today* **2008**, *136*, 76–83.

(10) Cheng, L.; Ge, Q. *J. Phys. Chem. C* **2008**, *112*, 16924–16931.

(11) Kwak, J. H.; Mei, D.; Yi, C.-W.; Kim, D. H.; Peden, C. H.; Allard, L. F.; Szanyi, J. *J. Catal.* **2009**, *261*, 17–22.

(12) Liu, Z.; Ma, L.; Junaid, A. S. M. *J. Phys. Chem. C* **2010**, *114*, 4445–4450.

(13) Mei, D.; Kwak, J. H.; Szanyi, J.; Ge, Q.; Peden, C. H. *Catal. Today* **2010**, *151*, 304–313.

(14) Vestreng, V.; Ntziachristos, L.; Semb, A.; Reis, S.; Isaksen, I. S. A.; Tarrasón, L. *Atmos. Chem. Phys.* **2009**, *9*, 1503–1520.

(15) Nova, I.; Castoldi, L.; Lietti, L.; Tronconi, E.; Forzatti, P. *Catal. Today* **2002**, *75*, 431–437.

(16) Mei, D.; Ge, Q.; Kwak, J. H.; Kim, D. H.; Szanyi, J.; Peden, C. H. F. *J. Phys. Chem. C* **2008**, *112*, 18050–18060.

(17) Szanyi, J.; Kwak, J. H.; Hanson, J.; Wang, C.; Szailer, T.; Peden, C. H. F. *J. Phys. Chem. B* **2005**, *109*, 7339–7344.

(18) Liotta, L.; Macaluso, A.; Arena, G.; Livi, M.; Centi, G.; Deganello, G. *Catal. Today* **2002**, *75*, 439–449.

(19) Takahashi, N.; Suda, A.; Hachisuka, I.; Sugiura, M.; Sobukawa, H.; Shinjoh, H. *Appl. Catal., B* **2007**, *72*, 187–195.

(20) Hirata, H.; Hachisuka, I.; Ikeda, Y.; Tsuji, S.; Matsumoto, S. *Top. Catal.* **2001**, *16–17*, 145–149.

(21) Andonova, S. M.; Şentürk, G. S.; Kayhan, E.; Özensoy, E. *J. Phys. Chem. C* **2009**, *113*, 11014–11026.

(22) Li, L.; Shen, Q.; Cheng, J.; Hao, Z. *Catal. Today* **2010**, *158*, 361–369.

(23) Andonova, S. M.; Şentürk, G. S.; Özensoy, E. *J. Phys. Chem. C* **2010**, *114*, 17003–17016.

(24) Miyoshi, N.; Matsumoto, S. *Sci. Technol. Catal.* **1998**, 245.

(25) Hohenberg, P.; Kohn, W. *Phys. Rev.* **1964**, *136*, B864–B871.

(26) Kohn, W.; Sham, L. J. *Phys. Rev.* **1965**, *140*, A1133–A1138.

(27) Perdew, J. P.; Burke, K.; Ernzerhof, M. *Phys. Rev. Lett.* **1996**, *77*, 3865–3868.

(28) Giannozzi, P. *J. Phys.: Condens. Matter* **2009**, *21*, 395502.

(29) Kokalj, A. *Comput. Mater. Sci.* **2003**, *28*, 155–168.

(30) Vanderbilt, D. *Phys. Rev. B* **1990**, *41*, 7892–7895.

(31) Monkhorst, H. J.; Pack, J. D. *Phys. Rev. B* **1976**, *13*, 5188–5192.

(32) Burdett, J. K.; Hughbanks, T.; Miller, G. J.; Richardson, J. W.; Smith, J. V. *J. Am. Chem. Soc.* **1987**, *109*, 3639–3646.

(33) Lazzeri, M.; Vittadini, A.; Selloni, A. *Phys. Rev. B* **2001**, *63*, 155409.

(34) Lazzeri, M.; Vittadini, A.; Selloni, A. *Phys. Rev. B* **2002**, *65*, 119901.

(35) Calatayud, M.; Minot, C. *Surf. Sci.* **2004**, *552*, 169–179.

(36) Marzari, N.; Vanderbilt, D.; Payne, M. C. *Phys. Rev. Lett.* **1997**, *79*, 1337–1340.

(37) Wyckoff, R. W. G. *Crystal Structures*; Wiley: New York, 1963.

(38) Schneider, W. F. *J. Phys. Chem. B* **2004**, *108*, 273–282.

(39) Broqvist, P.; Panas, I.; Grönbeck, H. *J. Phys. Chem. B* **2005**, *109*, 15410–15416.

(40) Tutuianu, M.; Inderwildi, O. R.; Bessler, W. G.; Warnatz, J. *J. Phys. Chem. B* **2006**, *110*, 17484−17492.

(41) Messmer, C.; Bilello, J. C. *J. Appl. Phys.* **1981**, *52*, 4623−4629.

(42) Jaccodine, R. J. *J. Electrochem. Soc.* **1963**, *110*, 524.

(43) Szanyi, J.; Kwak, J. H.; Kim, D. H.; Wang, X.; Hanson, J.; Chimentao, R. J.; Peden, C. H. F. *Chem. Commun.* **2007**, 984.

(44) Emmez, E.; Vovk, E. I.; Bukhtiyarov, V. I.; Ozensoy, E. *J. Phys. Chem. C* **2011**, *115*, 22438−22443.

(45) Grönbeck, H.; Broqvist, P.; Panas, I. *Surf. Sci.* **2006**, *600*, 403−408.

(46) Broqvist, P.; Grönbeck, H. *Surf. Sci.* **2006**, *600*, L214−L218.

(47) Sentürk, G. S.; Vovk, E. I.; Zaikovskii, V. I.; Say, Z.; Soylu, A. M.; Bukhtiyarov, V. I.; Ozensoy, E. *Catal. Today* **2012**, DOI: 10.1016/j.cattod.2011.12.006.

(48) Getman, R. B.; Schneider, W. F. *J. Phys. Chem. C* **2007**, *111*, 389−397.

(49) Ovesson, S.; Lundqvist, B. I.; Schneider, W. F.; Bogicevic, A. *Phys. Rev. B* **2005**, *71*, 115406.

(50) Smeltz, A.; Getman, R.; Schneider, W.; Ribeiro, F. *Catal. Today* **2008**, *136*, 84−92.